Multi-Mode Index Modulation Aided Multi-Band CAP With Balanced Pairwise Coding for Bandlimited VLC Systems

Yungui Nie, Chen Chen , Senior Member, IEEE, Zhihong Zeng , Xiaodi You , and Gangxiang Shen , Senior Member, IEEE

Abstract—In this paper, we for the first time propose and demonstrate a multi-mode index modulation aided multi-band carrierless amplitude and phase modulation (mCAP-MM) scheme for bandlimited visible light communication (VLC) systems. More specifically, the information bits of the proposed mCAP-MM scheme are conveyed through both multiple distinguishable modes and their full permutation indices. For mCAP-MM, due to the importance of choosing an appropriate constellation design strategy, we consider partitioning the circular (7,1)-quadrature amplitude modulation (QAM) constellation to obtain multiple distinguishable constellation modes. Moreover, an enhanced log-likelihood ratio (LLR) detector is also developed for mCAP-MM, which can solve the error propagation problem existed in the conventional LLR detector and achieve nearly optimal performance as the maximum likelihood (ML) detector but with a much lower complexity. In addition, aiming at the problem of signal-to-noise ratio (SNR) imbalance among different subbands due to the low-pass effect in practical VLC systems, a novel balanced pairwise coding (B-PWC) technique is further proposed and incorporated into the proposed mCAP-MM scheme. The feasibility and superiority of the proposed mCAP-MM scheme with enhanced LLR detection and B-PWC coding have been successfully verified by both simulations and experiments. Specifically, simulation results verify the superiority of mCAP-MM employing the designed multiple constellation modes and enhanced LLR detection over the additive white Gaussian noise (AWGN) channel, and then the validity of B-PWC in bandlimited m CAP-MM VLC systems is verified via proof-of-concept experiments. Experimental results demonstrate that a bandwidth extension of 19.9% can be achieved by the

Received 22 July 2024; revised 26 September 2024; accepted 18 October 2024. Date of publication 24 October 2024; date of current version 3 March 2025. This work was supported in part by the Postgraduate Research & Practice Innovation Program of Jiangsu Province under Grant KYCX24_3312, in part by the National Natural Science Foundation of China under Grant 62271091 and Grant 62001319, in part by Suzhou Science and Technology Bureau-Technical Innovation Project in Key Industries under Grant SYG202112, and in part by the Open Fund of IPOC (BUPT) under Grant IPOC2020A009. (Corresponding authors: Chen Chen; Gangxiang Shen.)

Yungui Nie, Xiaodi You, and Gangxiang Shen are with the Jiangsu New Optical Fiber Technology and Communication Network Engineering Research Center, Suzhou Key Laboratory of Advanced Optical Communication Network Technology, Institute for Broadband Research & Innovation (IBRI), Soochow University, Suzhou 215006, China, and also with the School of Electronic and Information Engineering, Soochow University, Suzhou 215006, China (e-mail: 20234028002@stu.suda.edu.cn; xdyou@suda.edu.cn; shengx@suda.edu.cn).

Chen Chen and Zhihong Zeng are with the School of Microelectronics and Communication Engineering, Chongqing University, Chongqing 400044, China (e-mail: c.chen@cqu.edu.cn; zhihong.zeng@cqu.edu.cn).

Color versions of one or more figures in this article are available at https://doi.org/10.1109/JLT.2024.3485961.

Digital Object Identifier 10.1109/JLT.2024.3485961

proposed 8CAP-MM with B-PWC in comparison to that with traditional PWC.

Index Terms—Carrierless amplitude and phase modulation, multiple-mode index modulation, pairwise coding, visible light communication (VLC).

I. INTRODUCTION

☐ INCE the spectrum resources of traditional radio frequency (RF) communication are limited and many frequency bands require licenses to be used, it is necessary to find more spectrum resources to meet more business needs and higher communication rates. However, the 400 THz-600 THz band used by visible light communication (VLC) systems contains sufficient and license-free spectrum resources. Therefore, VLC has great potential as an alternative to traditional RF communication, and is one of the key enabling technologies for the sixth generation (6G) mobile networks and the Internet of Things (IoT) systems [1], [2]. For VLC systems, as long as the speed of light intensity variation is high enough, the human eye cannot detect the flicker of light-emitting diode (LED) during the communication process. Moreover, photo-detectors (PDs) can detect these changes in brightness to enable data reception. Therefore, improving the communication rate and stability of VLC systems can simultaneously realize lighting and communication. In addition, practical VLC systems also have the advantages of high physical-layer security, and enhanced anti-electromagnetic interference capability [3].

However, practical VLC systems using LED as transmitter have a critical challenge, namely limited modulation bandwidth [4]. To mitigate the problems posed by this challenge, the analog/digital and pre-/post-equalization has been employed to extend the LED modulation bandwidth [5], [6], [7]. Moreover, some spectral efficient modulation techniques, such as orthogonal frequency division multiplexing (OFDM) and carrierless amplitude and phase modulation (CAP), have also been considered to improve the available data rate of VLC systems [8], [9], [10]. Compared with OFDM, CAP employs two mutually orthogonal digital filters, eliminating the discrete Fourier transform (DFT) and inverse discrete Fourier transform (IDFT) operations, so the implementation complexity of CAP is lower. By assigning different center frequencies to the digital filters, CAP realizes the signal transmission of multiple subbands, called multi-band

0733-8724 © 2024 IEEE. Personal use is permitted, but republication/redistribution requires IEEE permission. See https://www.ieee.org/publications/rights/index.html for more information.

CAP (mCAP) [11], [12]. Besides lower complexity, mCAP also enjoys the advantage of a much reduced peak-to-average power ratio (PAPR) in comparison to conventional OFDM [13], [14], [15].

In recent years, many researchers have considered introducing index modulation as a promising technique into mCAP systems to realize the expansion of subband index domain and obtain improved spectral efficiency (SE) or energy efficiency (EE). To be more specifically, mCAP with index modulation (mCAP-IM) has been proposed, which exists a problem that some subbands are in a silent state, resulting in underutilization of spectrum resources [16]. In order to make idle subbands also transmit constellation symbols to further improve SE, mCAP with dualmode index modulation (mCAP-DM) has been proposed [15], [17]. For mCAP-DM, the constellation symbols transmitted by the selected and remaining subbands are without any intersection to ensure the correct demodulation of additional index information. Moreover, the index modulation aided non-orthogonal m-CAP technique has also been considered [18]. On the basis of existing index modulation techniques, the multi-mode index modulation technique has been proposed and widely used in OFDM [19], [20], [21]. In multi-mode index modulation aided OFDM (OFDM-MM), the subcarriers of each subblock transmit different constellation modes, and the choice of multiple distinguishable constellation modes has a great influence on the system performance. Moreover, a high-dimensional multi-mode index modulation aided OFDM scheme based on geometric shaping has been proposed to enhance the tolerance to nonlinearity with the increase of the constellation dimension [22]. In [23], multi-mode index modulation has been applied to filter bank multi-carrier (FBMC) VLC system, and a group-interleaved precoding (GIP) technique has been proposed to enhance the performance of the system. In [24], two low-pass mitigation schemes including discrete Fourier transform (DFT) spreading and subblock interleaving have been evaluated and compared in bandlimited VLC systems using OFDM-MM.

So far, multi-mode index modulation has not yet been studied in bandlimited mCAP VLC systems. However, all index modulation aided mCAP schemes will be affected by the low-pass frequency response of practical VLC systems. The low-pass frequency response will lead to the unbalanced performance of different subbands, making each subband of mCAP suffer from a different power attenuation, which results in the signal-to-noise ratio (SNR) imbalance among different subbands. Similar to other transmission systems, the overall performance is usually determined by the worst subband. Therefore, solving the SNR imbalance problem among different subbands is quite necessary. Several low-pass induced SNR imbalance mitigation schemes have already been reported for VLC systems in the literature such as pre-equalization [6], [25], DFT spreading [24], [26] and pairwise coding (PWC) [27], [28]. Specifically, pre-equalization requires the feedback of channel frequency response at the transmitter side, while DFT spreading converts the multi-carrier/band signal into a quasi-single-carrier/band signal. In contrast, PWC reveals its potential for low-pass induced SNR imbalance mitigation due to its low computational complexity and excellent performance [15], [29], [30]. Nevertheless, conventional PWC

is only able to mitigate the SNR imbalance within the subcarrier/subband pair, while the SNR imbalance among different subcarrier/subband pairs still exists.

In this paper, for the first time to our knowledge, we consider the combination of multi-mode index modulation and mCAP to design a novel modulation scheme, namely multi-mode index modulation aided mCAP (mCAP-MM). An efficient constellation design using circular (7,1)-quadrature amplitude modulation (QAM) constellation is considered in mCAP-MM with the subblock size being n = 4 and the order of constellation mode being M = 2. Moreover, an enhanced log-likelihood ratio (LLR) detector is designed to solve the error propagation problem existed in the conventional LLR detector, which can achieve nearly optimal performance as the maximum likelihood (ML) detector at a lower complexity. Furthermore, a novel balanced PWC (B-PWC) technique is also designed to address the issue of SNR imbalance among different subbands. The performance of the proposed mCAP-MM scheme with B-PWC coding in bandlimited VLC systems is verified through both numerical simulations and hardware experiments.

II. PRINCIPLE OF mCAP-MM

A. Description of mCAP-MM

The scheme of extending two constellation modes to multiple constellation modes without any intersection, and sending the multiple constellation modes to different subbands, is introduced into mCAP for the first time to form a new multi-carrier modulation technique, which is called mCAP-MM. As for mCAP-MM, all subbands are required to be activated. The additional information attached to the subbands within each subblock mainly comes from the full permutations of these distinguishable modes, and thus the number of all possible transmission modes increases by factorial to improve the transmission efficiency of the system.

The mCAP-MM is built on the conventional mCAP architecture, whose transmitter and receiver in bandlimited VLC systems are depicted in Fig. 1(a) and (b), respectively. For the transmission of every mCAP block, as shown in Fig. 1(a), the total subbands have a count of variable m which are equally split into g subblocks, with each subblock containing n = m/gsubbands. The input B bits are also divided into q groups, with every group containing b = B/g bits. For the k-th (k = B/g) $1, \ldots, g$) subblock, the b bits are separated into two parts. More specifically, the first part of b_1 bits determines the order of the modes $\{\chi_1, \ldots, \chi_n\}$ that is employed by n individual subbands, where χ_{γ} with $\gamma \in \mathcal{W} (= \{1, \dots, n\})$ is an M-ary constellation employed by the γ -th subbands. The second part containing $b_2 = n \log_2(M)$ bits generates the transmission symbol vector $s^{(k)} = [s_1^{(k)}, \dots, s_n^{(k)}],$ which is transmitted over n subbands from the selected modes. Since n subbands assign different constellation modes, the assigned modes must be distinguishable from each other, which explains that the number of subbands within the subblock is equal to the number of constellation modes. Moreover, after dividing the nM-ary constellation, the n constellation modes can be obtained. Therefore, the b_1 bits

2055

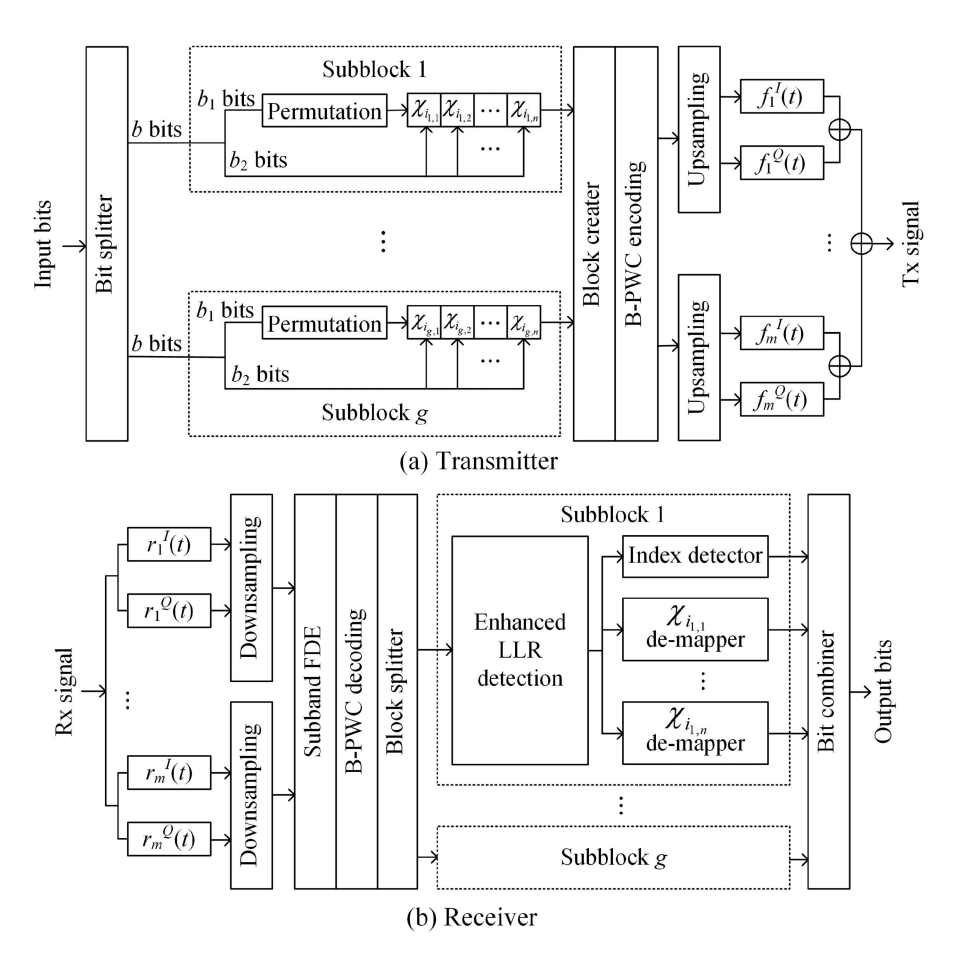


Fig. 1. Block diagram of mCAP-MM: (a) Transmitter and (b) receiver.

can only determine the order set of $\{\chi_{i_{k,1}}, \cdots, \chi_{i_{k,n}}\}$ through the permutation indices $I^{(k)} = [i_1^{(k)}, \dots, i_n^{(k)}]$, where $i_{k,\gamma} \in \mathcal{W}$ and $i_{\gamma}^{(k)} \in \{1, \dots, n\}$, which means that the maximum number of possible full permutations of χ_1, \dots, χ_n is n!, and $b_1 = \lfloor \log_2(n!) \rfloor$. In addition, we have $s_{\gamma}^{(k)} \in \chi_{i_{k,\gamma}}$ with $\gamma = 1, \dots, n$.

In addition, the mapping process between b_1 bits and the permutation indices is implemented through a permutation method [19]. The permutation method consists of the following contents. For any given natural number $Z \in [1, n! - 1]$, it is always possible to find a unique sequence $J = \{a_n, \ldots, a_1\}$, where $a_n, \ldots, a_1 \in \{1, \ldots, n\}$, to satisfy the following relation of Z:

$$Z = (a_n - 1) * (n - 1)! + \cdots + (a_2 - 1) * (1)! + (a_1 - 1) * 0!.$$
 (1)

The algorithm to obtain the J sequence can be simply described as follows: first choose the largest positive integer a_n to satisfy the inequality $(a_n-1)*(n-1)! \leq Z$, and then select the largest positive integer a_{n-1} in the same way to satisfy the inequality $(a_{n-1}-1)*(n-2)! \leq Z-(a_n-1)*(n-1)!$ and so on until we get a_1 . According to the obtained J sequence, the corresponding full permutation indices $I^{(k)}=[i_1^{(k)},\ldots,i_n^{(k)}]$ of the k-th subblock can be obtained. Moreover, an example of

mCAP-MM mapping for $b_1 = 4$ and n = 4 is illustrated in Table I. Since 4! = 24, eight illegal permutations are discarded. Although the permutation method imposes a bit of a computational burden, it is more efficient than look-up table for larger b_1 values.

After performing multi-mode index modulation, a block creater follows, which combines g subblocks to form a block. Subsequently, the B-PWC encoding is executed to mitigate the SNR imbalance among different subbands caused by the low-pass effect of practical VLC systems. The detailed process of the B-PWC encoding will be described later. The μ -th ($\mu=1,\ldots,m$) subband is taken as a demonstrative example, where upsampling is first performed and then the upsampled symbols are separated into real and imaginary parts via in-phase (I) and quadrature (Q) filters, respectively. The impulse response of a pair of I and Q filters can be respectively expressed as:

$$f_{\mu}^{I}(t) = g(t)\cos(2\pi f_{c,\mu}t),$$
 (2)

$$f_{\mu}^{Q}(t) = g(t)\sin(2\pi f_{c,\mu}t),$$
 (3)

where g(t) denotes the root raised cosine filter (RRCF), and $f_{c,\mu}$ is the center frequency of the μ -th subband. The choice of $f_{c,\mu}$ determines the orthogonality between the subbands. Finally, the transmitted mCAP-MM with B-PWC signal is generated through combining the m subband signals.

b_1 bits	$I^{(\beta)}$	Selected modes	b_1 bits	$I^{(\beta)}$	Selected modes
[0000]	$\{1, 2, 3, 4\}$	$\{\chi_1, \chi_2, \chi_3, \chi_4\}$	[1000]	$\{2, 3, 1, 4\}$	$\{\chi_2,\chi_3,\chi_1,\chi_4\}$
[0001]	$\{1, 2, 4, 3\}$	$\{\chi_1, \chi_2, \chi_4, \chi_3\}$	[1001]	$\{2, 3, 4, 1\}$	$\{\chi_2, \chi_3, \chi_4, \chi_1\}$
[0010]	$\{1, 3, 2, 4\}$	$\{\chi_1, \chi_3, \chi_2, \chi_4\}$	[1010]	$\{2,4,1,3\}$	$\{\chi_2, \chi_4, \chi_1, \chi_3\}$
[0011]	$\{1, 3, 4, 2\}$	$\{\chi_1,\chi_3,\chi_4,\chi_2\}$	[1011]	$\{2,4,3,1\}$	$\{\chi_2,\chi_4,\chi_3,\chi_1\}$
[0100]	$\{1, 4, 2, 3\}$	$\{\chi_1, \chi_4, \chi_2, \chi_3\}$	[1100]	${3,1,2,4}$	$\{\chi_3,\chi_1,\chi_2,\chi_4\}$
[0101]	$\{1,4,3,2\}$	$\{\chi_1,\chi_4,\chi_3,\chi_2\}$	[1101]	${3,1,4,2}$	$\{\chi_3,\chi_1,\chi_4,\chi_2\}$
[0110]	$\{2, 1, 3, 4\}$	$\{\chi_2,\chi_1,\chi_3,\chi_4\}$	[1110]	${3,2,1,4}$	$\{\chi_3,\chi_2,\chi_1,\chi_4\}$
[0111]	$\{2, 1, 4, 3\}$	$\{\chi_2,\chi_1,\chi_4,\chi_3\}$	[1111]	${3,2,4,1}$	$\{\chi_3,\chi_2,\chi_4,\chi_1\}$

 $\begin{tabular}{ll} TABLE I \\ A EXAMPLE OF mCAP-MM MAPPING TABLE FOR $b_1=4$ and $n=4$ \end{tabular}$

At the receiver, as shown in Fig. 1(b), the received signal goes through m pairs of matched filters to extract the real and imaginary parts of each subband. Moreover, the matched filter pair has the following relationship with the I and Q filters pair for the μ -th subband:

$$r^{\rm I}_{\mu}(t) = f^{\rm I}_{\mu}(-t),$$
 (4)

$$r_{\mu}^{Q}(t) = f_{\mu}^{Q}(-t).$$
 (5)

Subsequently, the obtained signal undergoes downsampling, subband frequency-domain equalization (FDE), B-PWC decoding, and block splitter, followed by enhanced LLR detection that detects signals independently for each subblock. The enhanced LLR detection involved will be discussed in detail later. After subblock detection, the b_1 bits and the constellation bits of different constellation modes are estimated via index detector and different $\chi_{ik,\gamma}$ de-mappers, respectively. Finally, the output bits are yielded through a bit combiner.

Therefore, for VLC systems using mCAP-MM with nM-QAM constellation, the SE of per subblock can be expressed by

$$SE_{m\text{CAP-MM}} = \frac{\lfloor \log_2(n!) \rfloor + n \log_2(M)}{n},$$
 (6)

where $\lfloor \cdot \rfloor$ represents the floor operator. It can be seen that the SE of mCAP-MM is determined only by the values of n and M. In contrast, the SE of each subblock for mCAP-IM with M-QAM constellation can be given by

$$SE_{m\text{CAP-IM}} = \frac{C + \eta \log_2(M)}{n},$$
 (7)

where $\mathcal{C} = \lfloor \log_2(C(n,\eta)) \rfloor$, with $C(\cdot,\cdot)$ denoting the binomial coefficient and η being the number of activated subbands out of n subbands in each subblock. For mCAP-DM, all subbands are divided into multiple subblocks, where the selected η subbands transmit M_{A} -QAM constellation and the remaining $n-\eta$ subbands transmit M_{B} -QAM constellation in each subblock. Furthermore, the order of the M_{A} -QAM and M_{B} -QAM constellations involved in mCAP-DM can be flexibly configured according to different requirements. For further comparison, the SE of each subblock for mCAP-DM with M_{A} -QAM and M_{B} -QAM constellations can be obtained as follows

$$SE_{m\text{CAP-DM}} = \frac{\mathcal{C} + \eta \log_2(M_{\text{A}}) + (n - \eta) \log_2(M_{\text{B}})}{n}.$$
 (8)

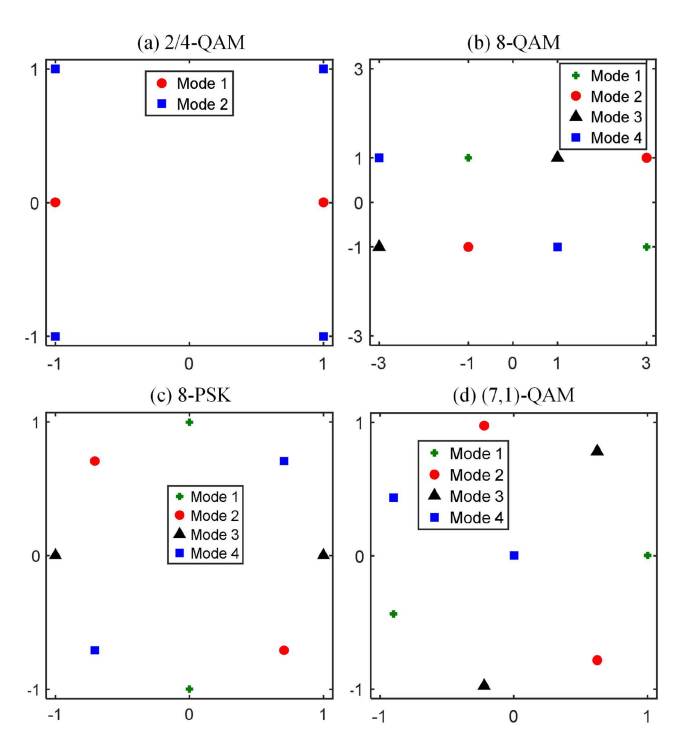


Fig. 2. Two constellation modes for mCAP-DM generated from (a) 2/4-QAM and four constellation modes for mCAP-MM generated from (b) 8-QAM, (c) 8-PSK and (d) circular (7,1)-QAM.

B. Constellation Design of mCAP-MM

The adopted multiple distinguishable constellation modes can greatly determine the performance of VLC systems employing mCAP-MM. The constellation diagram of the mCAP-MM, which includes n distinguishable constellation modes with the same constellation order M, can be obtained by dividing the nM-ary constellation. Each mode is required to contain Mconstellation points. In mCAP-MM, we consider the case of n=4 and M=2 to achieve the SE of 2 bits/s/Hz. Three 8-ary constellations including 8-QAM, 8-ary phase-shift keying (8-PSK) and circular (7,1)-QAM, are considered [31], [32], [33]. To get a fair comparison, $\eta = 2$ out of n = 4 subbands are selected to realize the same SE of 2 bits/s/Hz for mCAP-DM with 2-QAM and 4-QAM constellations. Fig. 2(a)–(d) show that the two constellation modes for mCAP-DM with 2/4-QAM, and four constellation modes for mCAP-MM with 8-QAM, 8-PSK and circular (7,1)-QAM, respectively. Besides dividing the common PSK or QAM constellations, constellation design

can also been realized via geometric constellation shaping [22], [34], which is beyond the scope of this current work and will be investigated in our future work.

C. Detector Design for mCAP-MM

1) ML Detector: Since each subblock is executed independently, maximum likelihood (ML) detection is performed on the received signal of each subblock to extract the estimates of the full permutation indices and the corresponding constellation symbols of each subband. The ML detection algorithm compares the received signal with all possible constellation symbols, and minimizes the value of the following formula to obtain the estimated value $\hat{\chi}^{(k)}$ of the transmitted symbol vector and the estimated value $\hat{I}^{(k)}$ of the full permutation indices for the k-th subblock, which can be formulated as

$$(\hat{\chi}^{(k)}, \hat{I}^{(k)}) = \arg\min_{\chi^{(k)}, I^{(k)}} ||y^k - \xi^k||^2,$$
 (9)

where $\hat{\chi}^{(k)} = [\hat{\chi}_{i_{k,1}} \cdots, \hat{\chi}_{i_{k,n}}]^T$ and $\hat{I}^{(k)} = [\hat{\imath}_1^{(k)}, \dots, \hat{\imath}_n^{(k)}]^T$, y^k denotes the received signal of the k-th subblock, and ξ^k presents the set of all possible permutations for the k-th subblock. There are $2^{\lfloor \log_2 n! \rfloor}$ possible cases in the full permutation indices of each subblock, and the transmitting signals of n subbands based on M-ary constellation contain M^n possible cases. Therefore, the complexity of ML detection is $o(2^{\lfloor \log_2 n! \rfloor} M^n)$ per subblock [19], which can be seen that when n is large, the complexity of ML detection is very high.

2) LLR Detector: Although the ML detector is optimal, it leads to high computational complexity. To reduce computational complexity, the LLR detector is considered. For LLR detection, letting $y^k(\varepsilon)$ $(k=1,\ldots,g;\varepsilon=1,\ldots,n)$ denote the received signal of the ε -th subband in the k-th subblock, the LLR value of the ε -th subband in the k-th subblock of mCAP-MM signal can be expressed as

$$L^{k}(\varepsilon,\tau) = \ln \frac{P(E^{k}|y^{k}(\varepsilon))}{P(E^{k}_{\perp}|y^{k}(\varepsilon))}, \tau = 1,\dots, n,$$
 (10)

where E^k presents the event of the ε -th subband using the τ -th constellation mode, and E^k_\perp represents the opposite event of E^k . Because of $P(E^k) \approx \frac{1}{n}$ and $P(E^k_\perp) \approx 1 - \frac{1}{n}$, (10) is further expressed as

$$L^{k}(\varepsilon,\tau) = \ln \sum_{\chi \in \chi_{\tau}} \exp\left(-\frac{1}{N_{0}} \left|y^{k} - \chi\right|^{2}\right) - \ln(n-1)$$
$$-\ln \sum_{\psi \neq \tau} \sum_{\chi \in \chi_{\psi}} \exp\left(-\frac{1}{N_{0}} \left|y^{k} - \chi\right|^{2}\right), \quad (11)$$

where N_0 is the noise power. A larger value of $L^k(\varepsilon,\tau)$ means that the probability of the ε -th subband using the τ -th constellation mode is greater. More specifically, starting from the first constellation mode, the subband index $\hat{\alpha}_1$ of the signal constellation employing the mode is determined according to the maximum value of $[L^k(1,1),\ldots,L^k(n,1)]^T$. After that, considering the second constellation mode, the subband index $\hat{\alpha}_2$ of the signal constellation using the mode is determined from the remaining n-1 subbands in the same way, and so on.

Therefore, the subband index $\{\hat{\alpha}_1,\dots,\hat{\alpha}_n\}$ corresponding to the n constellation modes can be obtained, and the estimated value of the full permutation indices is further obtained. However, in the LLR detection process, the subband index corresponding to the first constellation mode is first determined, and the subband index corresponding to the second constellation mode is determined according to the judgment result of the first constellation mode, and so on. The detection algorithm has the issue of error propagation. That is, if the judgment result of the first constellation mode is wrong, the judgment of the remaining constellation modes will be affected. Moreover, the complexity of LLR detection is $o(Mn^2/2 + Mn/2)$ per subblock [19].

3) Proposed Enhanced LLR Detector: In order to solve the error propagation issue of LLR detection, an enhanced LLR detector is further proposed. The enhanced LLR detector is an improved version of the LLR detector. For the enhanced LLR detector, according to (11), a larger value of $L^k(\varepsilon,\tau)$ means that the ε -th subband is more likely to adopt the τ -th constellation mode. To perform detection, firstly, n subbands are judged independently under the n constellation modes, and the LLR value L^k of the k-th subblock is obtained according to (11), which can be expressed as

$$L^{k} = \begin{bmatrix} L^{k}(1,1) & \dots & L^{k}(1,n) \\ \vdots & \ddots & \vdots \\ L^{k}(n,1) & \dots & L^{k}(n,n) \end{bmatrix}.$$
 (12)

Subsequently, the permutation index of n subbands using the corresponding constellation mode is determined by comparing the maximum value of each column of L^k . Finally, the obtained permutation index of n subbands is compared in pairs. As long as the same subband index appears in the comparison process, the subband is considered to be an error in judgment. The received signal of the error subband is extracted and ML detection is carried out separately to ensure the decision accuracy. Moreover, the complexity of enhanced LLR detection is Mn^2 per subblock.

4) Complexity Analysis: In this subsection, we summarize the computational complexity of the three detection algorithms including ML detector, LLR detector and enhanced LLR detector. Considering the computational complexity of each subblock as a performance measure, the values of ML detector, LLR detector and enhanced LLR detector can be calculated as $2^{\lfloor \log_2 n! \rfloor} M^n$, $Mn^2/2 + Mn/2$ and Mn^2 , respectively. Compared with ML detector, the enhanced LLR detector has a lower computational complexity. Moreover, the enhanced LLR detector solves the issue of error propagation that exists in LLR detector, which can achieve much better detection performance than the conventional LLR detector.

III. THE IMPROVEMENT OF PWC

A. Traditional PWC

Traditional PWC can reduce the impact of severe high-frequency attenuation on the overall system performance, which has the advantages of no coding overhead and low complexity. Because of the low-pass characteristic of practical VLC systems, the SNRs of the high-frequency subbands are usually lower than

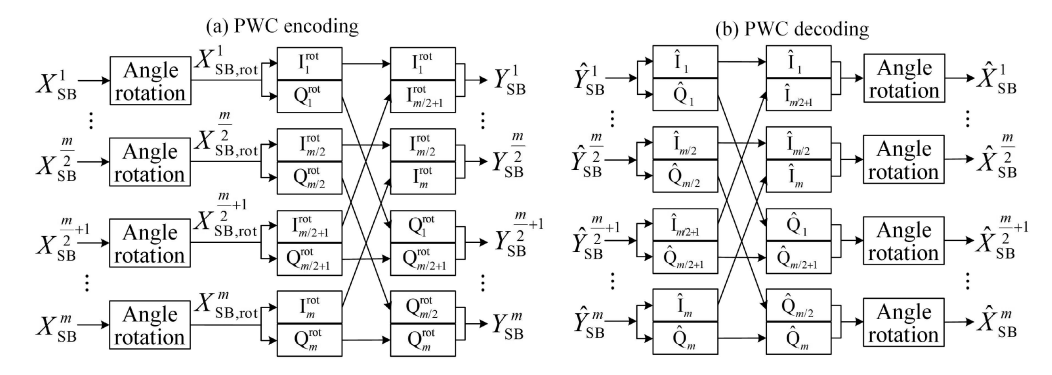


Fig. 3. Schematic diagrams of traditional PWC: (a) Encoding and (b) decoding.

that of the low-frequency subbands. The main idea of PWC is to transfer SNR imbalance to the in-phase and quadrature components of the transmitted complex symbols, and then the in-phase and quadrature components of the high-frequency and low-frequency subbands are interleaved to improve the overall performance of VLC systems.

In order to perform PWC, considering that the number of subbands m is even, m subbands are separated into two parts. More specifically, the first half of the m subbands from the first subband to the (m/2)-th subband is defined as the first part, and the second part has the second half of the m subbands from the (m/2+1)-th subband to the m-th subband, which are understood as the low-frequency part and the high-frequency part, respectively. Subsequently, the m/2 subband pairs are obtained by pairing the ς -th $(\varsigma=1,\ldots,m/2)$ subband of the first part with the $(m/2+\varsigma)$ -th subband of the second part. The schematic diagrams of the PWC encoding and decoding are illustrated in Fig. 3(a) and (b), respectively. The input complex signal of the β -th subband is denoted by $X_{\rm SB}^{\beta}={\rm I}_{\beta}+j{\rm Q}_{\beta}$ $(\beta=1,\ldots,m)$.

1) Encoding: As for PWC encoding in Fig. 3(a), firstly, the angle rotation is performed and the obtained rotated signal pair $X_{\mathrm{SB},rot}^{\varsigma}$ and $X_{\mathrm{SB},rot}^{\frac{m}{2}+\varsigma}$ can be expressed by

$$\begin{bmatrix} X_{\text{SB},rot}^{\varsigma} \\ X_{\text{SB},rot}^{\frac{m}{2}+\varsigma} \end{bmatrix} = \begin{bmatrix} I_{\varsigma} + jQ_{\varsigma} & -Q_{\varsigma} + jI_{\varsigma} \\ I_{\frac{m}{2}+\varsigma} + jQ_{\frac{m}{2}+\varsigma} & -Q_{\frac{m}{2}+\varsigma} + jI_{\frac{m}{2}+\varsigma} \end{bmatrix} \begin{bmatrix} \cos \theta \\ \sin \theta \end{bmatrix},$$
(13)

where θ is the rotation angle, and in previous studies of PWC, θ is set to 45° [28], [29]. Subsequently, the in-phase and quadrature components of all subbands are interleaved and the output signal pair $Y_{\rm SB}^{\varsigma}$ and $Y_{\rm SB}^{\frac{m}{2}+\varsigma}$ can be given by

$$\begin{bmatrix} Y_{\text{SB}}^{\varsigma} \\ Y_{\text{SB}}^{\frac{m}{2}+\varsigma} \end{bmatrix} = \begin{bmatrix} I_{\varsigma} + jI_{\frac{m}{2}+\varsigma} & -Q_{\varsigma} - jQ_{\frac{m}{2}+\varsigma} \\ Q_{\varsigma} + jQ_{\frac{m}{2}+\varsigma} & I_{\varsigma} + jI_{\frac{m}{2}+\varsigma} \end{bmatrix} \begin{bmatrix} \cos \theta \\ \sin \theta \end{bmatrix},$$
(14)

2) Decoding: For PWC decoding, as shown in Fig. 3(b), the corresponding received signals $\hat{Y}^1_{\rm SB},\ldots,\hat{Y}^m_{\rm SB}$ of m subbands independently execute the separation of the in-phase and quadrature parts, deinterleaving and angle rotation to obtain the estimates of the transmitted symbols $X^1_{\rm SB},\ldots,X^m_{\rm SB}$. It is worth noting that the rotation angle is the negative of θ , which is set to -45° . The estimated signal pair $\hat{X}^\varsigma_{\rm SB}$ and $\hat{X}^{\frac{m}{2}+\varsigma}_{\rm SB}$ can be represented by

$$\begin{bmatrix} \hat{X}_{\text{SB}}^{\varsigma} \\ \hat{X}_{\text{SB}}^{\frac{m}{2}+\varsigma} \end{bmatrix} = \begin{bmatrix} \hat{\mathbf{I}}_{\varsigma} + j\hat{\mathbf{I}}_{\frac{m}{2}+\varsigma} & \hat{\mathbf{I}}_{\frac{m}{2}+\varsigma} - j\hat{\mathbf{I}}_{\varsigma} \\ \hat{\mathbf{Q}}_{\varsigma} + j\hat{\mathbf{Q}}_{\frac{m}{2}+\varsigma} & \hat{\mathbf{Q}}_{\frac{m}{2}+\varsigma} - j\hat{\mathbf{Q}}_{\varsigma} \end{bmatrix} \begin{bmatrix} \cos\theta \\ \sin\theta \end{bmatrix}. (15)$$

B. Proposed B-PWC

In order to improve traditional PWC, a new B-PWC coding technique is proposed for the first time, which has a more obvious effect on solving SNR imbalance among different subbands due to the low-pass effect in practical VLC systems. As for B-PWC, m subbands are separated into two parts. The same as traditional PWC is that the first half of the m subbands

$$\begin{bmatrix} x_{\text{SB}}^{\zeta} \\ x_{\text{SB}}^{\frac{m}{4}+\zeta} \\ x_{\text{SB}}^{\frac{m}{2}+\zeta} \\ x_{\text{SB}}^{\frac{m}{2}+\zeta} \\ x_{\text{SB}}^{\frac{m}{2}+\zeta} \\ x_{\text{SB}}^{\frac{m}{2}+\zeta} \end{bmatrix} = \begin{bmatrix} I_{\zeta} + jI_{\frac{m}{2}-\zeta+1} & -(Q_{\zeta} + jQ_{\frac{m}{2}-\zeta+1}) \\ Q_{\frac{m}{4}-\zeta+1} + jQ_{\frac{m}{4}+\zeta} & I_{\frac{m}{4}-\zeta+1} + jI_{\frac{m}{4}+\zeta} \\ I_{\frac{m}{2}+\zeta} + jI_{m-\zeta+1} & -(Q_{\frac{m}{2}+\zeta} + jQ_{m-\zeta+1}) \\ Q_{\frac{3m}{4}-\zeta+1} + jQ_{\frac{3m}{4}+\zeta} & I_{\frac{3m}{4}-\zeta+1} + jI_{\frac{3m}{4}+\zeta} \end{bmatrix} \begin{bmatrix} \cos\vartheta \\ \sin\vartheta \end{bmatrix}, \zeta = \left\{1, \dots, \frac{m}{4}\right\},$$

$$\begin{bmatrix} Y_{\text{SB}}^{\zeta} \\ Y_{\text{SB}}^{\frac{m}{4}+\zeta} \\ Y_{\text{SB}}^{\frac{m}{4}+\zeta} \\ Y_{\text{SB}}^{\frac{m}{4}+\zeta} \\ Y_{\text{SB}}^{\frac{m}{4}+\zeta} \end{bmatrix} = \begin{bmatrix} I_{\zeta} + jI_{\frac{m}{2}+\zeta} & Q_{\frac{m}{2}-\zeta+1} + jQ_{m-\zeta+1} & -(Q_{\zeta} + I_{\frac{m}{2}-\zeta+1} + jQ_{\frac{m}{2}+\zeta} + jI_{m-\zeta+1}) \\ Q_{\frac{m}{4}-\zeta+1} + jQ_{\frac{3m}{4}-\zeta+1} & -(I_{\frac{m}{4}+\zeta} + jI_{\frac{3m}{4}+\zeta}) & I_{\frac{m}{4}-\zeta+1} - Q_{\frac{m}{4}+\zeta} + jI_{\frac{3m}{4}-\zeta+1} - jQ_{\frac{3m}{4}+\zeta} \\ I_{\frac{m}{2}-\zeta+1} + jI_{m-\zeta+1} & -(Q_{\zeta} + jQ_{\frac{m}{2}+\zeta}) & I_{\zeta} - Q_{\frac{m}{2}-\zeta+1} + jI_{\frac{m}{2}+\zeta} - jQ_{m-\zeta+1} \\ Q_{\frac{m}{4}+\zeta} + jQ_{\frac{3m}{4}+\zeta} & I_{\frac{m}{4}-\zeta+1} + jI_{\frac{3m}{4}-\zeta+1} & I_{\frac{m}{4}+\zeta} + Q_{\frac{m}{4}-\zeta+1} + jI_{\frac{3m}{4}+\zeta} + jQ_{\frac{3m}{4}-\zeta+1} \end{bmatrix} \begin{bmatrix} \cos^2\vartheta \\ \sin\vartheta^2\vartheta \\ \sin\vartheta^2\vartheta \end{bmatrix},$$

$$(16)$$

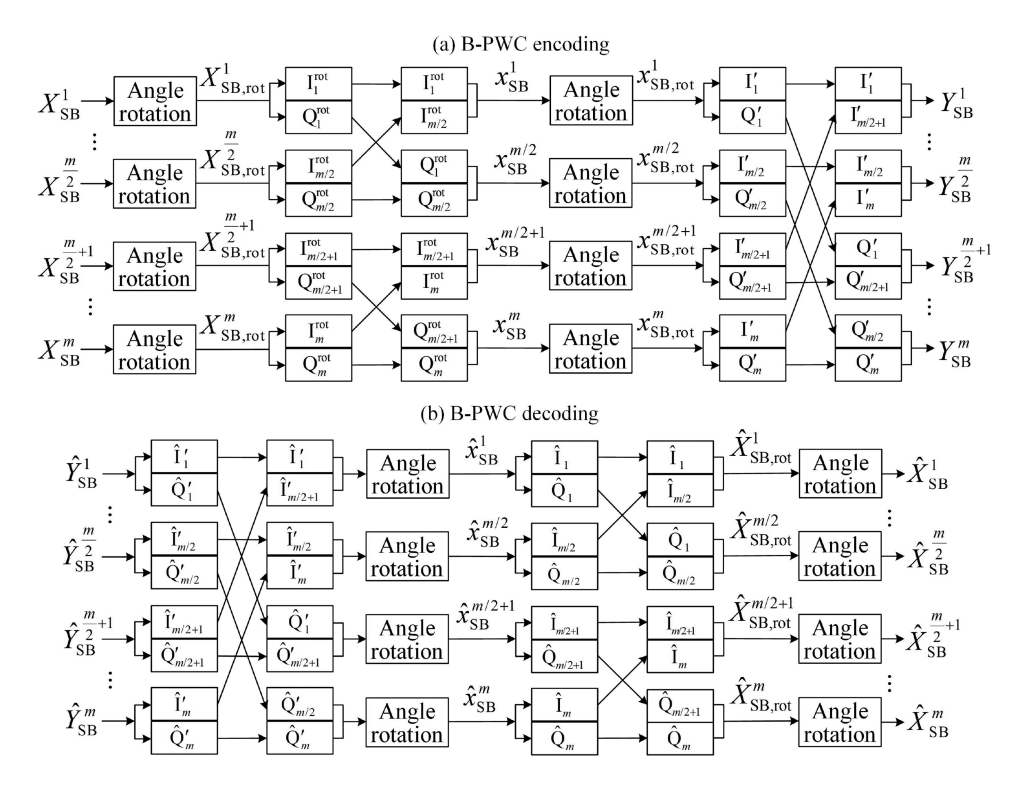


Fig. 4. Schematic diagrams of B-PWC: (a) Encoding and (b) decoding.

from the first subband to the (m/2)-th subband is defined as the first part, and the second part has the second half of the msubbands from the (m/2+1)-th subband to the m-th subband. After that, the m/2 subband pairs contain the m/4 subband pairs in the first part and the m/4 subband pairs in the second part. Specifically, the m/4 subband pairs are obtained by pairing the ζ -th ($\zeta = 1, \ldots, m/4$) subband with the $(m/2 - \zeta + 1)$ -th subband in the first part to alleviate the problem of SNR imbalance among different subbands in the low-frequency part, while the remaining m/4 subband pairs are obtained by pairing the $(m/2 + \zeta)$ -th subband with the $(m - \zeta + 1)$ -th subband in the second part to alleviate the problem of SNR imbalance in the high-frequency subbands. Subsequently, the regenerated msubbands perform a second-stage pairing, which is a specific process that the m/2 subband pairs are obtained by pairing the ς -th ($\varsigma = 1, \ldots, m/2$) subband of the first part with the $(m/2 + \varsigma)$ -th subband of the second part to further alleviate the problem of SNR imbalance among different subbands. It can be summarized as follows: the m subbands are first separated into two groups, and then the B-PWC coding is performed on the grouped subbands by employing the first-stage pairing and second-stage pairing described above. The schematic diagrams of the B-PWC encoding and decoding are illustrated in Fig. 4(a) and (b), respectively.

1) Encoding: For B-PWC encoding, as shown in Fig. 4(a), the input complex signals $X_{\rm SB}^1,\ldots,X_{\rm SB}^m$ of m subbands perform angle rotation first. Subsequently, the low-frequency and high-frequency subbands are interleaved separately to complete the first-stage pairing. Considering two regenerated signal pairs

 $x_{\rm SB}^{\zeta}, x_{\rm SB}^{\frac{m}{4}+\zeta}$ and $x_{\rm SB}^{\frac{m}{2}+\zeta}, x_{\rm SB}^{\frac{3m}{4}+\zeta}$ located in the low-frequency and high-frequency parts, respectively, the two signal pairs can be described in (16) shown at the bottom of previous page, where ϑ is the rotation angle which is also set to 45° . Subsequently, the regenerated signals $x_{\rm SB}^1, \ldots, x_{\rm SB}^m$ of m subbands execute the second-stage pairing. More specifically, the regenerated signals perform angle rotation at the angle ϑ of 45° and then pair the low-frequency and high-frequency subbands to obtain the B-PWC encoded signals. The two output signal pairs $Y_{\rm SB}^{\zeta}, Y_{\rm SB}^{\frac{m}{4}+\zeta}$ and $Y_{\rm SB}^{\frac{m}{2}+\zeta}, Y_{\rm SB}^{\frac{3m}{4}+\zeta}$ can be formulated as (17) shown at the bottom of previous page.

2) Decoding: The B-PWC decoding is the inverse process of B-PWC encoding. For B-PWC decoding, as shown in Fig. 4(b), the corresponding received signals $\hat{Y}^1_{SB},\ldots,\hat{Y}^m_{SB}$ execute deinterleaving corresponding to the second-stage pairing mentioned above, and angle rotation to obtain the m subbands signals $\hat{x}^1_{SB},\ldots,\hat{x}^m_{SB}$. Moreover, the rotation angle is the negative of ϑ . The estimated ς -th ($\varsigma=1,\ldots,m/2$) signal pair can be given by

$$\begin{bmatrix} \hat{x}_{\text{SB}}^{\varsigma} \\ \hat{x}_{\text{SB}}^{\frac{m}{2}+\varsigma} \end{bmatrix} = \begin{bmatrix} \hat{I}'_{\varsigma} + j\hat{I}'_{\frac{m}{2}+\varsigma} & \hat{I}'_{\frac{m}{2}+\varsigma} - j\hat{I}'_{\varsigma} \\ \hat{Q}'_{\varsigma} + j\hat{Q}'_{\frac{m}{2}+\varsigma} & \hat{Q}'_{\frac{m}{2}+\varsigma} - j\hat{Q}'_{\varsigma} \end{bmatrix} \begin{bmatrix} \cos\vartheta \\ \sin\vartheta \end{bmatrix}, \quad (18)$$

Subsequently, the obtained signals of m subbands perform deinterleaving corresponding to the first-stage pairing, and two signal pairs $\hat{X}_{\mathrm{SB,rot}}^{\zeta}$, $\hat{X}_{\mathrm{SB,rot}}^{\frac{m}{4}+\zeta}$ and $\hat{X}_{\mathrm{SB,rot}}^{\frac{m}{2}+\zeta}$, $\hat{X}_{\mathrm{SB,rot}}^{\frac{3m}{4}+\zeta}$ can be formulated as (19), as shown at the bottom of the next page. Finally, angle rotation is executed to recover the transmitted symbols $\hat{X}_{\mathrm{SB}}^{1},\ldots,\hat{X}_{\mathrm{SB}}^{m}$, and the two signal pairs $\hat{X}_{\mathrm{SB}}^{\zeta}$, $\hat{X}_{\mathrm{SB}}^{\frac{m}{4}+\zeta}$ and $\hat{X}_{\mathrm{SB}}^{\frac{m}{2}+\zeta}$,

 $\hat{X}_{\text{SB}}^{\frac{3m}{4}+\zeta}$ can be formulated as (20), as shown at the bottom of this page. It can be seen from Fig. 3 that conventional PWC can only mitigate the SNR imbalance within each subband pair (i.e., intra-pair SNR imbalance), while the SNR imbalance among different subband pairs (i.e., inter-pair SNR imbalance) still exists. In contrast, as shown in Fig. 4, the proposed balanced PWC technique can mitigate both intra-pair SNR imbalance and inter-pair SNR imbalance, resulting in a more balanced SNR distribution among all the subbands than that using conventional PWC.

C. Complexity Analysis

Here, we analyze and compare the computational complexity of traditional PWC and B-PWC. The implementation steps of the traditional PWC encoding, as shown in Fig. 3(a), consist of angle rotation and I/Q interleaving. According to the output signals of traditional PWC from (13), it takes 2 multiplications and 1 addition to compute each element, and there are 4 elements in the matrix, so the total number of calculations for a pair of subbands contains 8 multiplications and 4 additions. Moreover, considering that the number of subbands is m and m is even, the computational complexity of traditional PWC encoding includes $8 \times \frac{m}{2}$ multiplications and $4 \times \frac{m}{2}$ additions. For B-PWC, the implementation steps consist of the first-stage pairing and second-stage pairing, including two angle rotation and two I/Q interleaving operations. According to the output signals of B-PWC from (17), 3 multiplications and 2 additions are required to compute each element, and a pair of subbands contains 6 elements in the matrix, so the total number of computations is 18 multiplications and 12 additions in a pair of subbands. Therefore, the computational complexity of B-PWC encoding includes $18 \times \frac{m}{2}$ multiplications and $12 \times \frac{m}{2}$ additions. In addition, the decoding complexity and the encoding complexity of traditional PWC and B-PWC are the same, so the computational complexity of traditional PWC and B-PWC decoding is not described in this paper.

IV. SIMULATION RESULTS

In this section, numerical simulations are conducted to examine the performance of the proposed mCAP-MM with circular (7,1)-QAM employing enhanced LLR detector over the additive white Gaussian noise (AWGN) channel. In the simulations, the

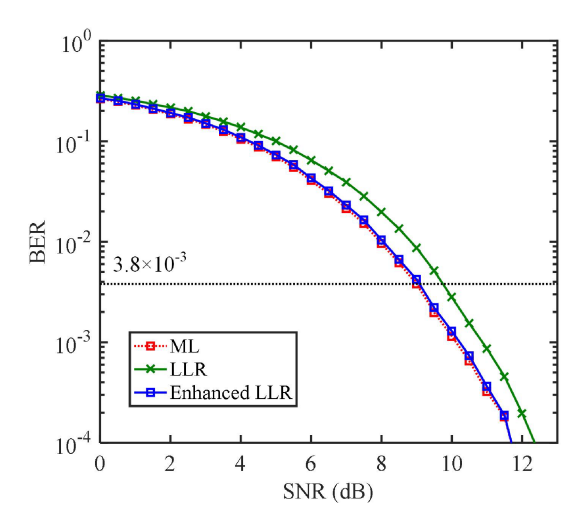


Fig. 5. Simulation BER vs. SNR for the proposed 8CAP-MM scheme employing ML detector, LLR detector and enhanced LLR detector over the AWGN channel.

size of each subblock in mCAP-MM is set to n=4. Moreover, each distinguishable constellation mode in the proposed mCAP-MM scheme has the same order, and the order is set to M=2. Therefore, according to (6), the corresponding SE is calculated as 2 bits/s/Hz. To make a fair comparison, mCAP, mCAP-IM and mCAP-DM are chosen as benchmark schemes. For mCAP-IM, the size of each subblock and the activated subbands in each subblock are set to n=4 and $\eta=2$, respectively, while all subbands are used to transmit information for mCAP-DM and the selected subbands in each subblock of length n=4 is $\eta=2$.

We first investigate the bit error rate (BER) performance of three detectors, including ML detector, conventional LLR detector and enhanced LLR detector, for the proposed mCAP-MM scheme over the AWGN channel. Fig. 5 shows the BER performance curves for mCAP-MM scheme employing the considered three detectors over the AWGN channel, where the number of subbands is set to m=8. As seen from Fig. 5, the enhanced LLR detector achieves nearly the same BER performance as the optimal ML detector, which has better BER performance compared with the conventional LLR detector. To be more specific, to reach the 7% forward error correction (FEC) coding limit of BER = 3.8×10^{-3} , the required SNRs for 8CAP-MM

$$\begin{bmatrix} \hat{X}_{\text{SB,rot}}^{\zeta} \\ \hat{X}_{\text{SB,rot}}^{\frac{M}{4}+\zeta} \\ \hat{X}_{\text{SB,rot}}^{\frac{M}{4}+\zeta} \\ \hat{X}_{\text{SB,rot}}^{\frac{M}{2}+\zeta} \end{bmatrix} = \begin{bmatrix} \hat{I}'_{\zeta} + j \hat{I}'_{\frac{m}{2}-\zeta+1} & \hat{I}'_{\frac{m}{2}+\zeta} + j \hat{I}'_{m-\zeta+1} \\ \hat{I}'_{\frac{3m}{4}-\zeta+1} + j \hat{I}'_{\frac{3m}{4}+\zeta} & -(\hat{I}'_{\frac{m}{4}-\zeta+1} + j \hat{I}'_{\frac{m}{4}+\zeta}) \\ \hat{Q}'_{\zeta} + j \hat{Q}'_{\frac{m}{2}-\zeta+1} & \hat{Q}'_{\frac{m}{2}+\zeta} + j \hat{Q}'_{m-\zeta+1} \\ \hat{Q}'_{\frac{3m}{4}-\zeta+1} + j \hat{Q}'_{\frac{3m}{4}+\zeta} & -(\hat{Q}'_{\frac{m}{4}-\zeta+1} + j \hat{Q}'_{\frac{m}{4}+\zeta}) \end{bmatrix} \begin{bmatrix} \cos \vartheta \\ \sin \vartheta \end{bmatrix},$$

$$\begin{bmatrix} \hat{X}_{\text{SB}}^{\zeta} \\ \hat{X}_{\text{SB}}^{\frac{m}{4}+\zeta} \\ \hat{X}_{\text{SB}}^{\frac{m}{4}+\zeta} \\ \hat{X}_{\text{SB}}^{\frac{m}{2}+\zeta} \\ \hat{X}_{\text{SB}}^{\frac{m}{2}+\zeta} \end{bmatrix} = \begin{bmatrix} \hat{I}'_{\zeta} + j \hat{I}'_{\frac{m}{2}-\zeta+1} & \hat{I}'_{m-\zeta+1} - j \hat{I}'_{\frac{m}{4}-\zeta+1} & \hat{I}'_{\frac{m}{4}-\zeta+1} + j \hat{I}'_{m-\zeta+1} - j \hat{I}'_{\frac{m}{4}-\zeta+1} \\ \hat{I}'_{\frac{3m}{4}-\zeta+1} + j \hat{I}'_{\frac{3m}{4}+\zeta} & -\hat{I}'_{\frac{m}{4}+\zeta} + j \hat{I}'_{\frac{m}{4}-\zeta+1} & \hat{I}'_{\frac{3m}{4}+\zeta} - \hat{I}'_{\frac{m}{4}-\zeta+1} - j \hat{I}'_{\frac{m}{4}-\zeta+1} - j \hat{I}'_{\frac{m}{4}-\zeta+1} - j \hat{I}'_{\frac{m}{4}-\zeta+1} \\ \hat{Q}'_{\zeta} + j \hat{Q}'_{\frac{m}{2}-\zeta+1} & \hat{Q}'_{m-\zeta+1} - j \hat{Q}'_{\frac{m}{2}+\zeta} & \hat{Q}'_{\frac{m}{2}+\zeta} + \hat{Q}'_{\frac{m}{2}-\zeta+1} + j \hat{Q}'_{\frac{m}{4}-\zeta+1} - j \hat{Q}'_{\frac{m}{4$$

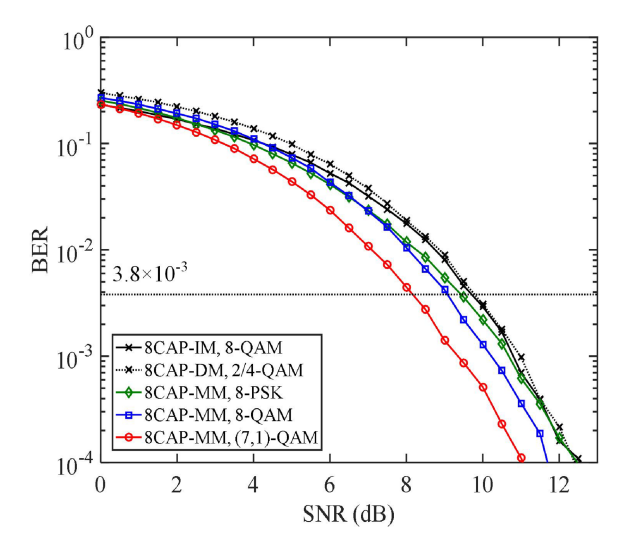


Fig. 6. Simulation BER vs. SNR for 8CAP-IM, 8CAP-DM and 8CAP-MM with 8-PSK, 8-QAM and circular (7,1)-QAM over the AWGN channel.

employing ML detector, conventional LLR detector and enhanced LLR detector are 9.0, 9.1 and 9.8 dB, respectively. It indicates that the difference in required SNRs between ML detector and enhanced LLR detector is only 0.1 dB, and the SNR gain of enhanced LLR detector in comparison to conventional LLR detector is 0.7 dB. This is because the proposed enhanced LLR detector is able to address the error propagation issue of the conventional LLR detector, which can achieve near optimal performance as the ML detector but with reduced complexity. Therefore, enhanced LLR detector is considered in the following for the proposed mCAP-MM scheme.

Subsequently, we investigate the BER performance of the proposed mCAP-MM scheme with 8-PSK, 8-QAM and circular (7,1)-QAM, and compare it with conventional mCAP-IM and mCAP-DM over the AWGN channel. Fig. 6 depicts the simulation BER versus SNR for mCAP-IM with 8-QAM, mCAP-DM with 2/4-QAM and mCAP-MM with 8-PSK, 8-QAM and circular (7,1)-QAM over the AWGN channel, where the number of subbands is fixed at m = 8. Compared with 8CAP-MM, 8CAP-IM and 8CAP-DM have worse BER performance. Moreover, it can be clearly observed that a proper constellation design can further improve the BER performance of 8CAP-MM. Specifically, to reach the 7% FEC coding limit of BER = 3.8×10^{-3} , the required SNRs of 8CAP-MM with 8-PSK, 8-QAM and circular (7,1)-QAM are 9.4, 9.1 and 8.2 dB, respectively. As a result, SNR gains of 1.2 and 0.9 dB can be achieved by 8CAP-MM with circular (7,1)-QAM in comparison to 8CAP-MM with 8-PSK and 8-QAM, respectively. Therefore, mCAP-MM with circular (7,1)-QAM achieves the best BER performance among all the mCAP-MM schemes.

We further compare the peak-to-average power ratio (PAPR) performance of mCAP and mCAP-MM with circular (7,1)-QAM. Fig. 7 presents the complementary cumulative distribution function (CCDF) versus PAPR for mCAP and mCAP-MM, where the number of subbands considered is m = 4, 8, 12 and 16. Although the number of subbands in mCAP is assumed to be

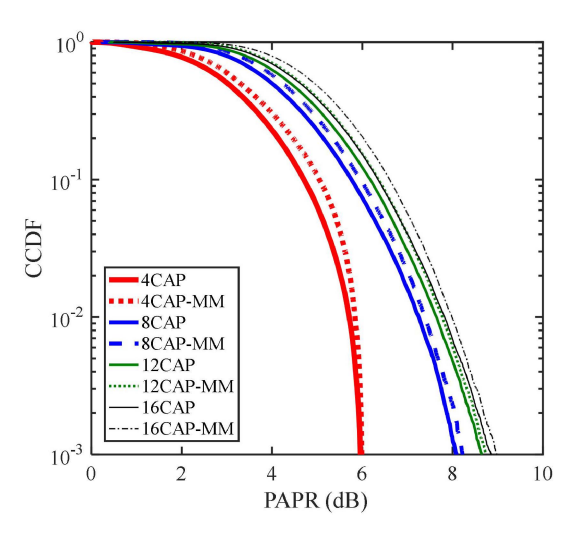


Fig. 7. PAPR comparison of mCAP and mCAP-MM with circular (7,1)-OAM

4, 8, 12 and 16, the proposed mCAP-MM scheme is generally applicable to mCAP with an arbitrary number of subbands. It can be clearly seen that mCAP-MM achieves nearly the same PAPR performance as mCAP. As an example, at a probability of 10^{-3} , the PAPR values of 8CAP and 8CAP-MM are 8.1 and 8.2 dB, respectively. It can be further observed that with the increase of the number of subbands, the PAPR performance deteriorates gradually. More specifically, the PAPR values of 4CAP-MM, 8CAP-MM, 12CAP-MM and 16CAP-MM at a probability of 10^{-3} are 6.0, 8.2, 8.7 and 9.0 dB, respectively. It indicates that the PAPR of 4CAP-MM is 2.2 dB lower than that of 8CAP-MM, while the PAPR of 8CAP-MM is 0.5 dB lower than that of 12CAP-MM. Therefore, when m increases in the range of 4 to 16 with a step of 4, the PAPR gap is gradually decreased.

V. EXPERIMENTAL RESULTS

In this section, we evaluate the performance of the proposed mCAP-MM scheme in practical bandlimited VLC systems via hardware experiments. Moreover, circular (7,1)-QAM is considered in the proposed mCAP-MM scheme, and enhanced LLR detector is integrated into mCAP-MM to realize better system performance. For comparison, traditional mCAP, mCAP-IM and m CAP-DM are considered in the performance evaluation.

Fig. 8 gives the experimental setup of a point-to-point VLC system using the Tx module and the inset (a) of Fig. 8 is the photo of the overall experimental system. Firstly, the transmitted signal is obtained offline via MATLAB. Subsequently, the obtained transmitted signal is uploaded into an arbitrary waveform generator (AWG, Rigol DG2102) with a maximum sampling rate of 60 MSa/s. Here, different signal bandwidths are obtained by varying the AWG sampling rate. To drive the Tx module (HCCLS2021MOD01-TX), the 12V voltage applied to the DC input is combined with the AWG output signal. The Tx module is embedded with a blue mini-LED (HCCLS2021CHI03) with an emission wavelength of 459.3 nm and an optical power of 18.5 mW. Moreover, the peak-to-peak voltage of the Tx module is 250 mV and the detailed description of the Tx module can be

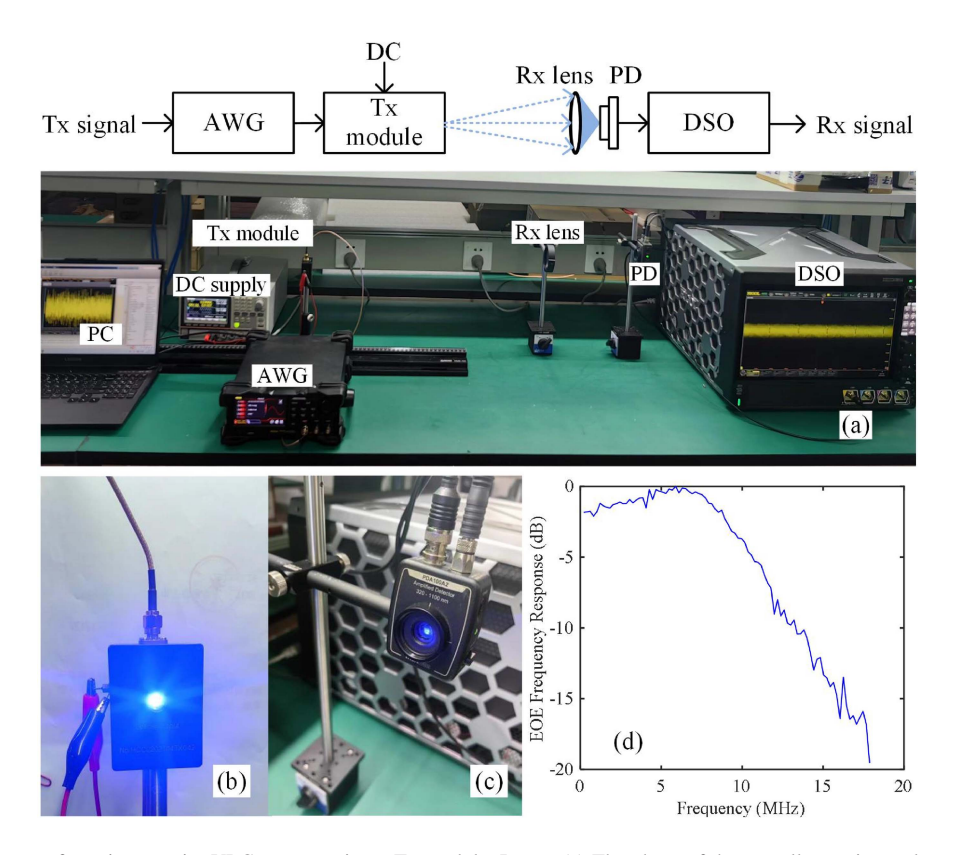


Fig. 8. Experimental setup of a point-to-point VLC system using a Tx module. Insets: (a) The photo of the overall experimental system, (b) the photo of Tx module, (c) the photo of PD and (d) the measured frequency response of VLC system.

seen in [35]. The light from the Tx module is transmitted in the air, and the transmission distance is 80 cm. At the receiver, a PD (Thorlabs PDA100A2) with the bandwidth of 11 MHz and the active area of 75.4 mm² is used to receive the signal transmitted from the Tx module. Moreover, a Rx lens is adopted to align the Tx module and the PD so as to obtain a relatively high SNR. The insets (b) and (c) in Fig. 8 are the photos of the Tx module and the PD, respectively. Subsequently, the signals received by PD are captured employing a digital storage oscilloscope (DSO, Rigol DS70504). Finally, the recorded signals are processed offline via MATLAB. In addition, the inset (d) in Fig. 8 shows the measured frequency response of the experimental VLC system. It can be clearly observed that a significant low-pass effect of the experimental system is demonstrated and the corresponding -3 dB bandwidth of about 9 MHz is measured. Fig. 9(a) and (b) show the measured I-V and P-I curves of the blue mini-LED adopted in the Tx module, respectively. We can see that the LED suffers from notable nonlinearity. In the experiments, the DC bias current adopted in the Tx module is set to 110mA.

Fig. 10 compares the transmitted and received spectra of 4CAP, 8CAP, 12CAP and 16CAP. As shown in Fig. 10(a) and (b), we can observed that the power of high-frequency components of the received spectrum for 4CAP is greatly attenuated and a power attenuation of about 17 dB is found, which is mainly caused by the low-pass frequency response as shown in Fig. 8(d). Moreover, each subband encounters a different power, resulting in a different SNR for each subband. With the increase of the number of subbands, the low-pass effect in each subband

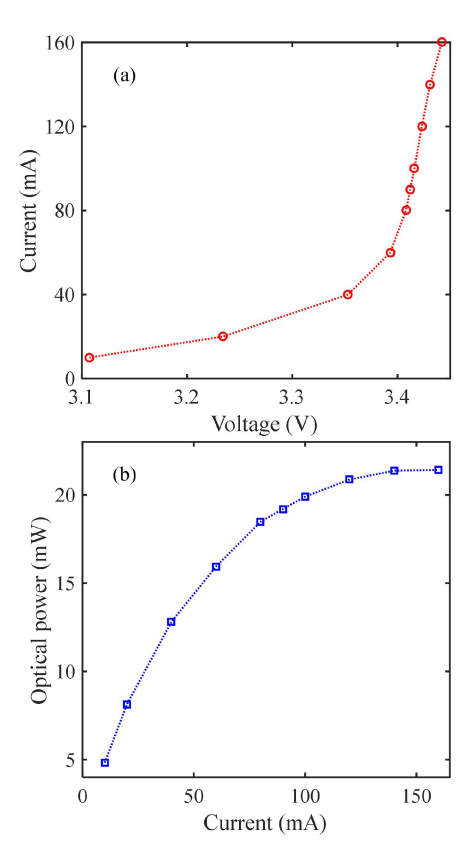


Fig. 9. Measured (a) I-V and (b) P-I curves of the blue mini-LED adopted in the Tx module.

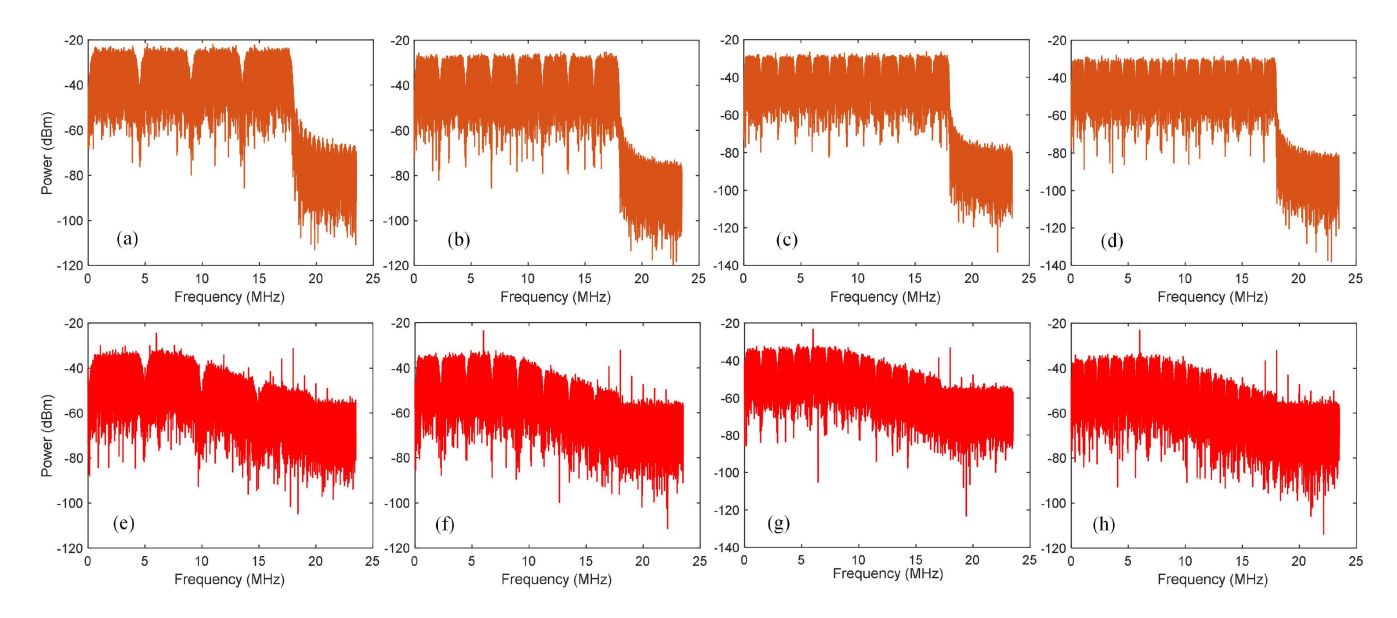


Fig. 10. Transmitted spectrum of (a) 4CAP, (b) 8CAP, (c) 12CAP and (d) 16CAP, and received spectrum of (e) 4CAP, (f) 8CAP, (g) 12CAP and (h) 16CAP.

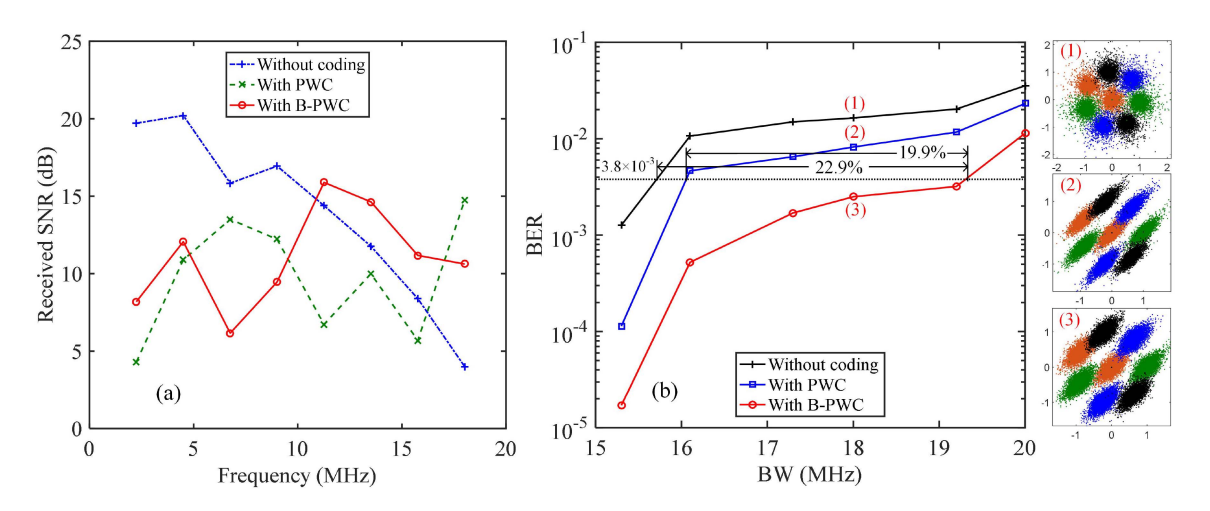


Fig. 11. (a) Received SNR of 8CAP-MM without coding, with PWC and with B-PWC, and (b) experimental BER vs. bandwidth for 8CAP-MM without coding, with PWC and with B-PWC. Insets (1)–(3) show the corresponding constellation diagrams.

gradually decreases, while the SNR imbalance among different subbands still exists.

The received SNRs of 8CAP-MM without coding, with PWC and with B-PWC schemes are shown in Fig. 11(a), where the signal bandwidth considered is 18 MHz. It can be clearly found that the received SNR of 8CAP-MM without coding gradually decreases with the increase of frequency, which is mainly affected by the frequency response of the system as shown in Fig. 8(d). Because the overall performance of the system is typically determined by its weakest subband, the adoption of an effective coding technique is of great significance. It can also be observed that compared with 8CAP-MM without coding, both 8CAP-MM with PWC and with B-PWC schemes make the distribution of the received SNR greatly flattened in the frequency domain, and the received SNR of the high-frequency subbands of 8CAP-MM without coding scheme is significantly

improved. Moreover, the B-PWC technique has a more uniform distribution of received SNR in comparison to the traditional PWC. Subsequently, Fig. 11(b) shows the experimental BER versus bandwidth for 8CAP-MM without coding, with PWC and with B-PWC. As we can see, the BER performance of 8CAP-MM without coding, with PWC and with B-PWC gradually deteriorates with the increase of bandwidth. More specifically, the maximum bandwidths that can be transmitted by 8CAP-MM without coding, with PWC and with B-PWC are 15.7, 16.1 and 19.3 MHz, respectively. It indicates that the bandwidth extensions of 3.6 and 3.2 MHz are respectively obtained by 8CAP-MM with B-PWC in comparison to 8CAP-MM without coding and with PWC, which are corresponding to 22.9% and 19.9% extensions of bandwidth. Therefore, the proposed B-PWC for m CAP-MM is the best choice to alleviate the SNR imbalance caused by the low-pass effect of practical VLC

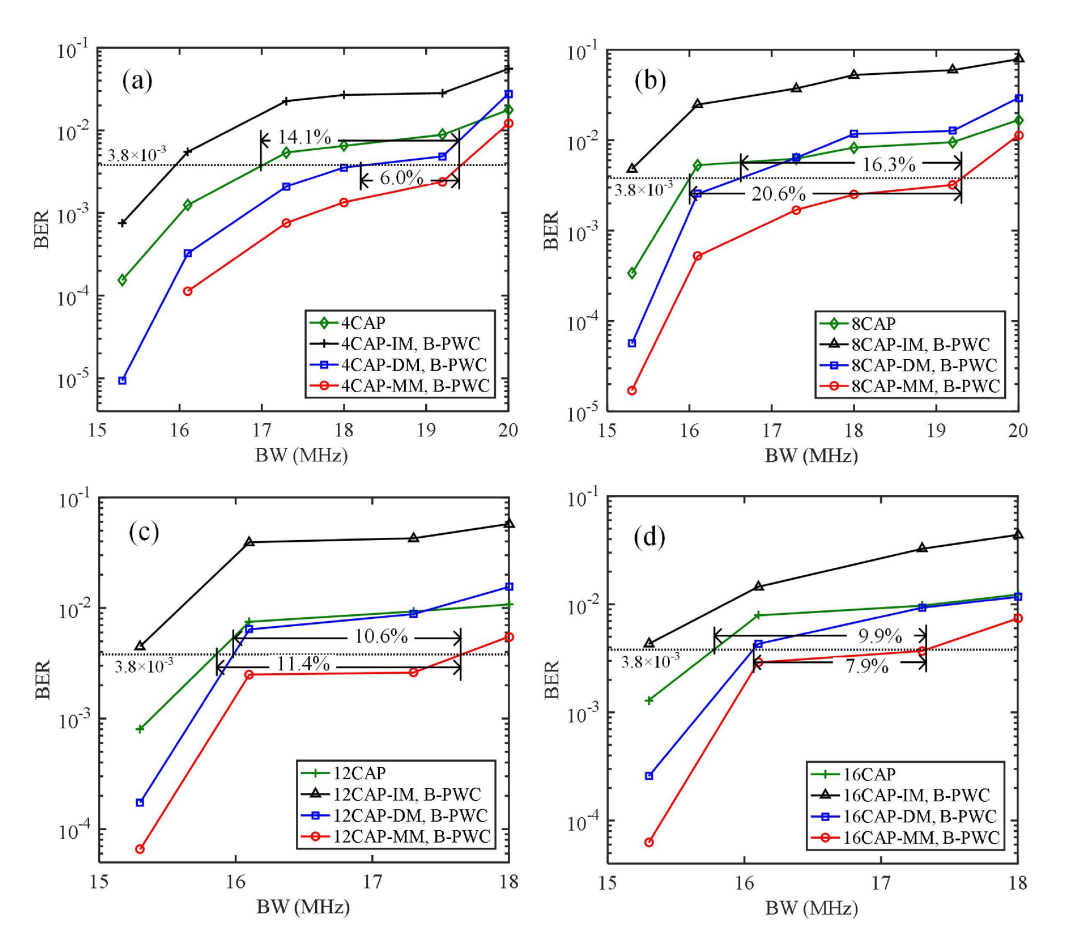


Fig. 12. Experimental BER vs. bandwidth for different schemes based on (a) 4CAP, (b) 8CAP, (c) 12CAP and (d) 16CAP.

systems. Moreover, the corresponding constellation diagrams for 8CAP-MM without coding, with PWC and with B-PWC, considering the case of the bandwidth of 18 MHz, are respectively depicted in insets (1)-(3) in Fig. 11. We can clearly see that compared with 8CAP-MM without coding and with PWC, the constellation of that with B-PWC is more convergent, which indicates that the obtained BER performance is better.

Fig. 12 illustrates the experimental BER versus bandwidth for mCAP, mCAP-IM with B-PWC, mCAP-DM with B-PWC and mCAP-MM with B-PWC, where the number of subbands considered is m = 4, 8, 12 and 16. It can be seen that the BER performance of mCAP, mCAP-IM with B-PWC, mCAP-DM with B-PWC and mCAP-MM with B-PWC under different subbands gradually deteriorates with the increase of bandwidth. To be more specific, for different schemes based on 4CAP, as shown in Fig. 12(a), to reach the 7% FEC coding limit of BER = 3.8×10^{-3} , the maximum bandwidths that can be transmitted by 4CAP, 4CAP-IM with B-PWC, 4CAP-DM with B-PWC and 4CAP-MM with B-PWC are respectively 17.0, 16.0, 18.3 and 19.4 MHz, which indicates that 4CAP-MM with B-PWC can obtain 14.1% and 6.0% extensions of bandwidth in comparison to 4CAP and 4CAP-DM with B-PWC, respectively. For different schemes based on 8CAP, as shown in Fig. 12(b), the BER of 8CAP-IM with B-PWC cannot reach the FEC limit of 3.8×10^{-3} within the considered bandwidth range, while

the maximum bandwidths that can be transmitted by 8CAP, 8CAP-DM with B-PWC and 8CAP-MM with B-PWC are 16, 16.6 and 19.3 MHz, respectively. As a result, 8CAP-MM with B-PWC can obtain 20.6% and 16.3% extensions of bandwidth in comparison to 8CAP and 8CAP-DM with B-PWC, respectively. Moreover, for different schemes aided 12CAP and 16CAP, as respectively shown in Fig. 12(c) and (d), the BERs for both 12CAP-IM and 16CAP-IM with B-PWC cannot reach the FEC limit of 3.8×10^{-3} within the considered bandwidth range. More specifically, 12CAP-MM with B-PWC can obtain 11.4% and 10.6% extensions of bandwidth in comparison to 12CAP and 12CAP-DM with B-PWC, respectively. In addition, 16CAP-MM with B-PWC can obtain 9.9% and 7.9% extensions of bandwidth in comparison to 16CAP and 16CAP-DM with B-PWC, respectively. According to Fig. 12(a)–(d), we can conclude that the BER performance of mCAP-MM deteriorates with the increase of subband number, mainly because the corresponding PAPR value increases with the increase of subband number, and the signal of high PAPR can be affected by the nonlinearity existed in the practical VLC systems. Moreover, among the subband numbers of m = 4, 8, 12 and 16, 8CAP-MM with B-PWC obtains the largest extension of bandwidth.

Fig. 13 shows the experimental BER versus subband number for mCAP, mCAP-IM with B-PWC, mCAP-DM with B-PWC and m CAP-MM with B-PWC, where the signal bandwidth

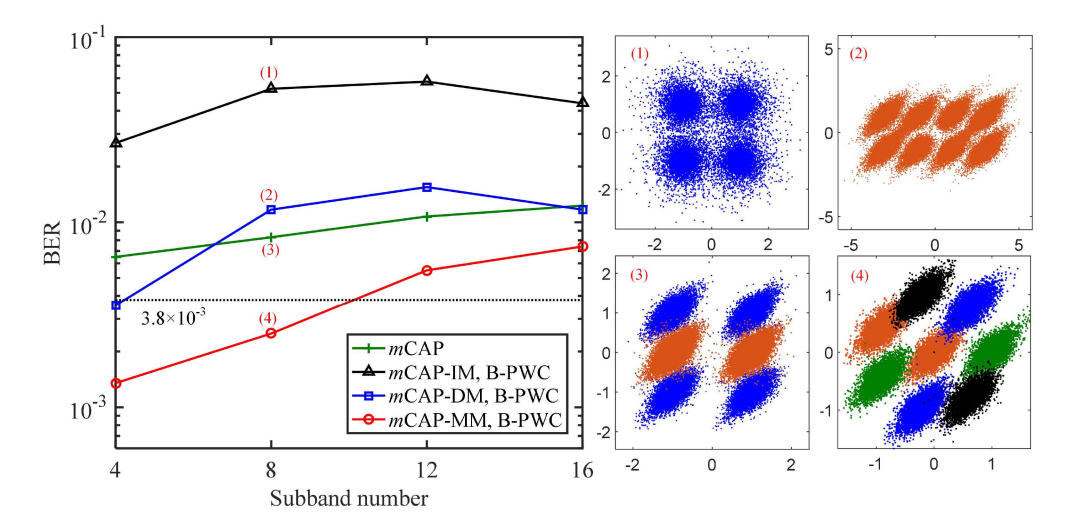


Fig. 13. Experimental BER vs. subband number for different schemes. Insets (1)-(4) show the corresponding constellation diagrams.

is fixed at 18 MHz. As we can see, to reach the 7% FEC coding limit of BER = 3.8×10^{-3} , mCAP and mCAP-IM with B-PWC cannot transmit signals in subband numbers of 4 to 16, while mCAP-DM with B-PWC can transmit signals in subband number of 4, and mCAP-MM with B-PWC can transmit signals in subband number increases from 4 to 16, the BER difference between mCAP and mCAP-MM with B-PWC decreases. Moreover, the corresponding constellation diagrams for 8CAP, 8CAP-IM with B-PWC, 8CAP-DM with B-PWC and 8CAP-MM with B-PWC are depicted in insets (1)-(4) in Fig. 13, respectively. It can be clearly seen from the insets that compared with the adopted constellations by 8CAP, 8CAP-IM, 8CAP-DM, the constellation points of 8CAP-MM with B-PWC are more concentrated.

VI. CONCLUSION

In this paper, a novel mCAP-MM scheme in bandlimited VLC systems has been proposed, which conveys information bits through both multiple distinguishable modes and the corresponding full permutation indices. For mCAP-MM with the subblock size being n = 4 and the order of constellation mode being M=2, an efficient constellation design of circular (7,1)-QAM constellation is considered. Moreover, an enhanced LLR detector is proposed to solve the error propagation problem existed in the conventional LLR detector, which can achieve nearly optimal performance as the ML detector at a lower complexity. In order to alleviate the problem of SNR imbalance among different subbands caused by the low-pass effect in bandlimited VLC systems, a B-PWC technique is also proposed and introduced into the proposed mCAP-MM scheme. The obtained simulation and experimental results verify the superiority of the proposed mCAP-MM using enhanced LLR detector and B-PWC for bandlimited VLC systems. The experimental results show that the use of B-PWC for 8CAP-MM can obtain a significant bandwidth extension of 19.9% in comparison to the traditional PWC. Therefore, the proposed m CAP-MM scheme with B-PWC coding can be a promising candidate for bandlimited VLC systems.

REFERENCES

- N. Chi, Y. Zhou, Y. Wei, and F. Hu, "Visible light communication in 6G: Advances, challenges, and prospects," *IEEE Veh. Technol. Mag.*, vol. 15, no. 4, pp. 93–102, Dec. 2020.
- [2] H. Zhou, M. Zhang, and X. Ren, "Design and implementation of wireless optical access system for VLC-IoT networks," *J. Lightw. Technol.*, vol. 41, no. 8, pp. 2369–2380, Apr. 2023.
- [3] T. Komine and M. Nakagawa, "Fundamental analysis for visible-light communication system using LED lights," *IEEE Trans. Consum. Electron.*, vol. 50, no. 1, pp. 100–107, Feb. 2004.
- [4] S. Rajagopal, R. D. Roberts, and S.-K. Lim, "IEEE 802.15.7 visible light communication: Modulation schemes and dimming support," *IEEE Commun. Mag.*, vol. 50, no. 3, pp. 72–82, Mar. 2012.
- [5] H. L. Minh et al., "100-Mb/s NRZ visible light communications using a postequalized white LED," *IEEE Photon. Technol. Lett.*, vol. 21, no. 15, pp. 1063–1065, Aug. 2009.
- [6] C. Chen et al., "Digital pre-equalization for OFDM-based VLC systems: Centralized or distributed?," *IEEE Photon. Technol. Lett.*, vol. 33, no. 19, pp. 1081–1084, Oct. 2021.
- [7] Y. F. Liu, Y. C. Chang, C. W. Chow, and C. H. Yeh, "Equalization and pre-distorted schemes for increasing data rate in in-door visible light communication system," presented at the Opt. Fiber Commun. Conf., Los Angeles, CA, USA, Mar. 6–10, 2011, Paper JWA83.
- [8] M. Z. Afgani, H. Haas, H. Elgala, and D. Knipp, "Visible light communication using OFDM," in Proc. Int. Conf. Testbeds Res. Infrastructures Develop. Netw. Communities, 2006, pp. 1–6.
- [9] Y. Nie et al., "0.5-bit/s/Hz fine-grained adaptive OFDM modulation for bandlimited underwater VLC," Opt. Exp., vol. 32, no. 3, pp. 4537–4552, Jan. 2024.
- [10] N. Bamiedakis, R. V. Penty, and I. H. White, "Carrierless amplitude and phase modulation in wireless visible light communication systems," *Philos. Trans. Roy. Soc. A*, vol. 378, no. 2169, Mar. 2020, Art. no. 20190181.
- [11] M. I. Olmedo et al., "Multiband carrierless amplitude phase modulation for high capacity optical data links," *J. Lightw. Technol.*, vol. 32, no. 4, pp. 798–804, Feb. 2014.
- [12] P. A. Haigh et al., "Multi-band carrier-less amplitude and phase modulation for bandlimited visible light communications systems," *IEEE Wireless Commun.*, vol. 22, no. 2, pp. 46–53, Apr. 2015.
- [13] F. Wu et al., "Performance comparison of OFDM signal and CAP signal over high capacity RGB-LED-based WDM visible light communication," *IEEE Photon. J.*, vol. 5, no. 4, Aug. 2013, Art. no. 7901507.
- [14] N. Chi, Y. Zhou, S. Liang, F. Wang, J. Li, and Y. Wang, "Enabling technologies for high-speed visible light communication employing CAP modulation," *J. Lightw. Technol.*, vol. 36, no. 2, pp. 510–518, Jan. 2018.
- [15] Y. Nie, Z. Wei, Y. Yang, X. Deng, M. Liu, and C. Chen, "Pairwise coded mCAP with chaotic dual-mode index modulation for secure bandlimited VLC systems," *Photonics*, vol. 9, no. 3, Feb. 2022, Art. no. 141.
- [16] K. O. Akande and W. O. Popoola, "Subband index carrierless amplitude and phase modulation for optical communications," *J. Lightw. Technol.*, vol. 36, no. 18, pp. 4190–4197, Sep. 2018.

- [17] K. O. Akande and W. O. Popoola, "Enhanced subband index carrierless amplitude and phase modulation in visible light communications," *J. Lightw. Technol.*, vol. 37, no. 23, pp. 5867–5874, Dec. 2019.
- [18] Z. Wang, J. Zhang, Z. He, P. Zou, and N. Chi, "Subcarrier index modulation super-Nyquist carrierless amplitude phase modulation for visible light communication systems," *J. Lightw. Technol.*, vol. 39, no. 20, pp. 6420–6433, Oct. 2021.
- [19] M. Wen, E. Basar, Q. Li, B. Zheng, and M. Zhang, "Multiple-mode orthogonal frequency division multiplexing with index modulation," *IEEE Trans. Commun.*, vol. 65, no. 9, pp. 3892–3906, Sep. 2017.
- [20] J. Li et al., "Composite multiple-mode orthogonal frequency division multiplexing with index modulation," *IEEE Trans. Commun.*, vol. 22, no. 6, pp. 3748–3761, Jun. 2023.
- [21] M. Wen, Q. Li, E. Basar, and W. Zhang, "Generalized multiple-mode OFDM with index modulation," *IEEE Trans. Commun.*, vol. 17, no. 10, pp. 6531–6543, Oct. 2018.
- [22] J. Ma, Z. Qi, J. Lu, J. Liu, N. Jia, and M. Luo, "Performance enhanced HD-MMIM-OFDM based on geometric shaping," *Opt. Fiber Technol.*, vol. 87, Oct. 2024, Art. no. 103938.
- [23] H. Wen, H. Chen, Q. Chen, K. Liu, C. Chen, and D. Mo, "Performance enhancement of multiple-mode FBMC-IM VLC systems with group-interleaved precoding," *Opt. Exp.*, vol. 32, no. 9, pp. 15801–15812, Apr. 2024.
- [24] F. Ahmed, J. Chen, S. Savović, and C. Chen, "Performance evaluation of OFDM with multi-mode index modulation in bandlimited low-pass VLC systems," in *Proc. Int. Conf. Robot.*, *Automat. Intell. Control*, 2023, pp. 399–403.
- [25] L. C. Mathias, J. C. M. Filho, and T. Abrao, "Predistortion and pre-equalization for nonlinearities and low-pass effect mitigation in OFDM-VLC systems," *Appl. Opt.*, vol. 58, no. 19, pp. 5328–5338, Jul. 2019.

- [26] F. Ahmed, Y. Nie, C. Chen, M. Liu, P. Du, and A. Alphones, "DFT-spread OFDM with quadrature index modulation for practical VLC systems," Opt. Exp., vol. 29, no. 21, pp. 33027–33036, 2021.
- [27] J. Boutros and E. Viterbo, "A power-and bandwidth-efficient diversity technique for the Rayleigh fading channel," *IEEE Trans. Inf. Theory*, vol. 44, no. 4, pp. 1453–1467, Jul. 1998.
- [28] J. He, J. He, and J. Shi, "An enhanced adaptive scheme with pairwise coding for OFDM-VLC system," *IEEE Photon. Technol. Lett.*, vol. 30, no. 13, pp. 1254–1257, Jul. 2018.
- [29] H. G. Olanrewaju, J. Thompson, and W. O. Popoola, "Pairwise coding for MIMO-OFDM visible light communication," *IEEE Trans. Wireless Commun.*, vol. 19, no. 2, pp. 1210–1220, Feb. 2020.
- [30] J. Wang, C. Chen, B. Deng, Z. Wang, M. Liu, and H. Y. Fu, "Enhancing underwater VLC with spatial division transmission and pairwise coding," *Opt. Exp.*, vol. 31, no. 10, pp. 16812–16832, May 2023.
- [31] J. Zhao, C. Qin, M. Zhang, and N. Chi, "Investigation on performance of special-shaped 8-quadrature amplitude modulation constellations applied in visible light communication," *Photon. Res.*, vol. 4, no. 6, pp. 249–256, Oct. 2016.
- [32] C. Chen, Y. Nie, F. Ahmed, Z. Zeng, and M. Liu, "Constellation design of DFT-S-OFDM with dual-mode index modulation in VLC," *Opt. Exp.*, vol. 30, no. 16, pp. 28371–28384, Jul. 2022.
- [33] T. Mao, R. Jiang, and R. Bai, "Optical dual-mode index modulation aided OFDM for visible light communications," *Opt. Commun.*, vol. 391, pp. 37–41, May 2017.
- [34] Y. Zhao et al., "Enhancing OFDM with index modulation using heuristic geometric constellation shaping and generalized interleaving for underwater VLC," Opt. Exp., vol. 32, no. 8, pp. 13720–13732, 2024.
- [35] C. Chen, Y. Nie, X. Zhong, M. Liu, and B. Zhu, "Characterization of a practical 3-m VLC system using commercially available Tx/Rx modules," in *Proc. Asia Commun. Photon. Conf.*, 2021, pp. 1–3.